Research results on biomagnetic imaging of the lung tumors

Laurel O. Sillerud[a,b], Sorin G. Popa[* a], Evangelos A. Coutsias[c], Daniel Sheltraw[e], Dean Kuethe[d], Natalie Adolphi[d]

[a]Feldmatech, Inc., 10734 Stone Hedge Ct. NW, Albuquerque, NM 87114
[b]Dept. of Biochemistry and Molecular Biology, Univ. of New Mexico, Albuquerque, NM 87131
[c]Dept. Of Mathematics, Univ. of New Mexico, Albuquerque, NM 87131
[d]New Mexico Resonance, 2301 Yale Blvd SE, Suite C-1, Albuquerque, NM 87106
[e]Helen Wills Neuroscience Institute, 132 Barker Hall MC 3190, University of California, Berkeley, Berkeley, CA 94720

ABSTRACT

Recent results on the development and implementation of a novel technology for lung tumor detection and imaging is presented. This technology offers high-sensitivity imaging of magnetic nanoparticles to provide specific diagnostic images of early lung tumors and potential distant metastases. Recent developments in giant magnetostrictive (GMS) or magnetic shape memory (MSM) materials have led to the possibility of developing small, low-cost, room-temperature, portable, high-sensitivity, fiber-optic sensors capable of robustly detecting magnetic nanoparticles, without direct contact with the skin. Magnetic nanoparticles are conjugated with antibodies, which target them to lung tumors.

A prototype fiber-optic biomagnetic sensor, based on giant magnetostrictive or magnetic shape memory materials, with the requisite sensitivity to image the magnetic signals generated by antibody-labeled magnetic nanoparticles in lung tumors has been built and calibrated. The uniqueness of the biomagnetic sensor lies in the fact that it offers high sensitivity at room temperature, and is not a SQUID-based system. The results obtained during the process of choosing the right magnetostrictive materials are presented. Then, for the construction of an accurate image of the lung tumor, the optimum spatial distribution of one-channel sensors and nanoparticle polarization has been analyzed.

Keywords: magnetometer, medical imaging, lung tumor, magnetic nanoparticles, antibodies

1. INTRODUCTION

Lung cancer is one of the leading causes of cancer-related death in the United States. One of the difficulties associated with the diagnosis of lung cancer is that there are four major histological types of lung tumors, with markedly different prognoses. These types are generally distinguished into two treatment groups as either Small Cell Lung Cancer (SCLC), comprising 25% of the tumors, or Non-Small Cell Lung Cancer (NSCLC), comprising the remaining 75%. NSCLC consists of squamous-cell carcinoma, adenocarcinoma, and Large-cell carcinoma. The fact that the death rate for lung cancer is so high is a reflection of the suboptimal state of current therapeutic approaches. For the NSCLC group of patients, successful therapies center on early detection and surgery since metastases occur later than with SCLC. For patients with the most limited stage of NSCLC at the time of initial diagnosis 5-year cure rates are ~50% [1]. For patients with more-advanced, nonresectable initial NSCLC, and with recurrent disease, chemotherapy and irradiation are employed, but long-term response rates are only 35% with a median survival time of only 25 weeks[2]. The clinical course and response to treatment of SCLC is very different from that for NSCLC. This cancer is one of the most metastatic of all solid tumors, and is extremely lethal[3]. Tumor spread occurs so early in the course of the disease that surgery is seldom used as a primary approach even for patients with no objective signs of metastasis at the time of initial diagnosis[4]. This highly-lethal cancer has among the highest initial sensitivity among solid tumors to combination chemotherapy[5] so that early detection could be crucial.

However, without early detection, recurrent and resistant disease virtually always ensues and the 5-year survival rate is only 5%, with an average survival time of 13 months[5]. Clearly, early diagnosis of the primary lesion, and any attending

---

* spopa@unm.edu, Telephone: (505) 922-1954

metastases, is critical to any rational plan to address the treatment of lung cancer. It has been estimated that early diagnosis could rescue up to 85% of lung cancer patients from the grim statistics presented above. This is where our magnetic imaging of lung tumors will have its greatest impact.

A high-sensitivity imaging of magnetic nanoparticles to provide specific diagnostic images of early lung tumors and potential distant metastases is currently being developed. Exciting recent developments in giant magnetostrictive (GMS) or magnetic shape memory (MSM) materials have led to the possibility of developing small, low-cost, room-temperature, portable, high-sensitivity, fiber-optic array sensors capable of robustly detecting magnetic nanoparticles, without direct contact with the skin[6,7]. Magnetic nanoparticles are conjugated with antibodies that target them to lung tumors.

The uniqueness of this biomagnetic sensor array lies in the fact that it offers high sensitivity at room temperature, and is not a SQUID-based system. SQUIDs (superconducting quantum interference devices) must operate at liquid helium temperatures (~4 K), which require bulky cryostats, and they consume expensive, non-renewable helium. From a commercial point of view, it is projected that our sensors could be produced at costs significantly lower than SQUID-based systems, and will incur substantially lower maintenance costs due to the absence of a cryogenic support system. We anticipate that this relative ease of deployment will lead to the rapid expansion of our fiber-optic magnetometer arrays in clinical practice.

1. Antibodies to lung tumors

The histologic classification of pulmonary neoplasms can have important implications regarding appropriate management of patients. Although the histologic classification of lung tumors is predominantly based on morphology, studies with immunohistochemistry[8] have shown that differential diagnosis of the various forms of lung cancer can be performed with antibodies. In particular, among NSCLC cases, 99% were positive for either keratin 34βE12, keratin 7 or B72.3, and among neuroendocrine carcinomas (SCLC), 84% were chromogranin positive[8]. CD56, or neural cell adhesion molecule (NCAM), is widely expressed by small cell carcinomas, and other tumors of neuroendocrine origin. Investigators using antibodies against CD56 to measure the surface concentration of CD56 in 27 lung tumors found that there was a 100 to 1000–fold increase in the amount of CD56 on the surface of SCLC tumors compared with that of matched isotype controls[9]. Antibodies against CD56 localized in the tumors of lung cancer patients[10] and were successfully used to eliminate tumor cells of neuroendocrine origin[11] without harming normal tissues. Specific binding to tumor cells in bone marrow, liver, and lung was observed. Since NCAM is distributed in the heart and peripheral nervous system, patients were examined for cardio- and neuro-toxicity. Cardiac function remained normal and no patient developed clinically significant neuropathy[12]. Thus, antibodies are available which will specifically target lung tumors, and can differentiate SCLC from NSCLC in vivo.

2. Magnetic Nanoparticles and Antibody-labeled Magnetic Nanoparticles

Magnetic nanoparticles are manufactured from ferromagnetic materials, but are so small that the individual particles are superparamagnetic, not ferromagnetic. The difference is that ferromagnetic materials retain a permanent magnetic moment, but paramagnetic materials only acquire a magnetic moment when placed into an external magnetic field. For this reason the magnetic nanoparticles do not clump together in solution. In order to detect the nanoparticles, we must first magnetize them in an external field. The magnetization of the nanoparticles will then proceed to decay (relax) once the external field is removed. The characteristics of this relaxation process are well-understood. These particles are so small (10-500 nm) that they undergo collisions with water molecules, which causes the magnetization of free particles to rotationally reorient on a time scale which is characteristic of Brownian motion. For nanoparticles free in solution, this time is of the order of nanoseconds. The relaxation time, $\tau_N = \tau_0 e^{-\Delta E/kT}$, where τ_0 is a constant ~ 10^{-9} s, ΔE is the magnetization energy barrier ~ 5 x 10^3 JV/m3, V is the particle volume (m^3), k is the Boltzmann constant (1.38 x 10^{-23} J/K), and T = 300 K. This exponential function predicts that the relaxation time is such a strong function of the particle volume that a change in diameter of only a factor of two from 25 to 50 nm produces a million-fold change in the relaxation time (from microseconds to minutes). This also predicts that if the nanoparticles are then bound to a lung tumor cell, the effective volume of the particle increases so much that the relaxation time increases from microseconds to many seconds, by the Neel mechanism. In this way, the magnetization of the free nanoparticles decays so quickly, that the only residual magnetization in the body arises from the nanoparticles bound to the tumor. The result is that the free nanoparticles produce no long-lasting magnetization signal[13] and hence no background, while the nanoparticles bound to the tumor remain magnetized for detection. The ratio of the magnetizations of the bound to the free particles easily exceeds one million to one. The strength of the field from the magnetic nanoparticles depends on their number, density, the value of the polarizing field, and the time elapsed after polarization. Typical values for the nanoparticle fields are of the order of 50-500 pT. These values are well within the operating range anticipated for our fiber-optic magnetometer array.

Since the success of this research depends upon the use of antibodies to specifically target magnetic nanoparticles to lungs tumors, we will briefly review the evidence that antibodies can indeed be tagged to nanoparticles, and that these function as expected. Remsen et al.[14] used periodate and cyanoborohydride reduction to directly conjugate L6 tumor-specific antibodies to dextran-containing nanoparticles, which then were successfully employed in tumor detection using MRI. In separate results, we have shown that we can indeed label anti-PSMA antibodies with nanoparticles, and that these particles specifically bind to, and can be imaged on, prostate cancer cells. A similar approach was taken for imaging the lung cancer cells.

2. MATERIALS AND TECHNOLOGY

Our novel approach for medical imaging consists of the measurement of the magnetic field produced by magnetic nanoparticles bound to organs or tissues within a living body. For the lung tumor imaging we chose to initially detect and image lung tumors induced in nude rats. There are several technologies to measure magnetic fields, but not all of them are suitable for medical imaging applications. These technologies can be classified as either non-optical or optical magnetic field sensing systems.

The most common magnetostrictive materials used for magnetic sensing are Terfenol-D and Metglas. The sensitivity of Metglas is in the range of 10^{-9} T. The sensitivity of our system can be adjusted either by changing the length of the magnetostrictive material rods or by using more sensitive magnetostrictive materials. Using longer rods is not suitable, though, when the sensor needs to be miniaturized for incorporation within an array. Therefore, a more sensitive material was used. For example, a Metglas-type material manufactured by UNITIKA Co., Japan, shows one order of magnitude better sensitivity. We believe that by using our technology the sensitivity of Metglas-type materials can be increased up to 10^{-15} T. However, we also considered the newly developed Magnetic Shape Memory (MSM) materials, which are more sensitive at very weak magnetic fields. In MSM materials the magnetic field moves microscopic parts of the material (so-called twins) that create a net shape change of the material. Magnetic fields produce a strain 50-100 times larger than traditional giant magnetostrictive materials.

The magnetic fields which emanate from the nanoparticles are much smaller (50-500 pT) than the background magnetic field from the Earth, which has a value of 50 microTesla. However, the Earth's field varies only slowly over time or over distances less than a few meters, so that this field acts only as a DC offset to any time-dependent biomagnetic field measurement, and can be removed from the measurement by operating the sensors as gradiometers. The fields from magnetic nanoparticles are at least as large as any arising from the body itself. From MRI studies, it is known that magnetic susceptibility gradients exist within the human body. The air-tissue interface is responsible for the largest of these, which can be as large as 50 pT/cm. We were able ameliorate these static effects through simple motion control. Our measurements were time-dependent, with coherent signal detection, so that these static effects only contribute to the magnetic background offset and are to be removed in our self-shielded sensor array.

In our feasibility studies, Metglas, Terfenol-D and NiMnGa (MSM material) were used as magnetic field sensor materials. Light from a laser diode was generated using a commercial driver module, and modulated at 1 kHz using the internal phase and frequency reference of a lock-in amplifier. The diode current and temperature were controlled by the driver module. We had available up to 300 mW of light at $\lambda = 1550$ nm, but in our experience, we were able to perform excellent studies with light levels of only 10 mW. One single-channel detector was amplified, so we have used optical attenuators to reduce the light from the interferometer to avoid saturation of the detector.

We have been working with samples of MSM (NiMnGa) material provided by Adaptmat, Finland where the maximum strain of 4.86 % corresponds to a sample length change of 729 μm. Our interferometer can measure changes in the optical path length of approximately 0.01 λ so with λ = 1550 nm, this translates into a path length change of 15 nm. It should be noted that the strain *versus* field curves have three distinct regions characterized by quite different sensitivities to the field variation. These regions, which differ according to the slope of the curves, are summarized in Table I, below.

Table I. Magnetic characteristics of MSM (NiMnGa) materials.

Region	***PreLoad (MPa)***	***Slope (μm/Gauss)***
A (0-26 kA/m)	1.2	3.85
A (0-72 kA/m)	1.5	2.68
A (0-151 kA/m)	1.8	1.92
B (~26 kA/m)	1.2	870,700.00
B (~72 kA/m)	1.5	1,020,000.00
B (~151 kA/m)	1.8	1,300,700.00
C (26-65 kA/m)	1.2	~800.00
C (72-136 kA/m)	1.5	~800.00
C (151-211 kA/m)	1.8	~800.00

The highest sensitivity arises in region B, where with a minimum strain of 15 nm, we calculate a minimum detectable field of ~1.1-1.7 pTesla, depending on the preload value. An examination of the maximum strain as a function of preload value showed (Figure 1) that the preload only reduced the maximum strain value attainable, and from the results shown in Fig. 2, it became clear that the position of the slope change (shown as the position of the "knee" in the curve in Fig. 2) varied with the preload in an undesirable way. Therefore we chose to operate the MSM material without a preload in order to increase the maximum strain attainable, and to be able to operate in the highest sensitivity region without having to bias the material with an applied static field independent of the measured field. By using this operating mode, we calculated that we could detect a ~10 % lower B_{min} than with a preload (B_{min} ~ 1.0 pT).

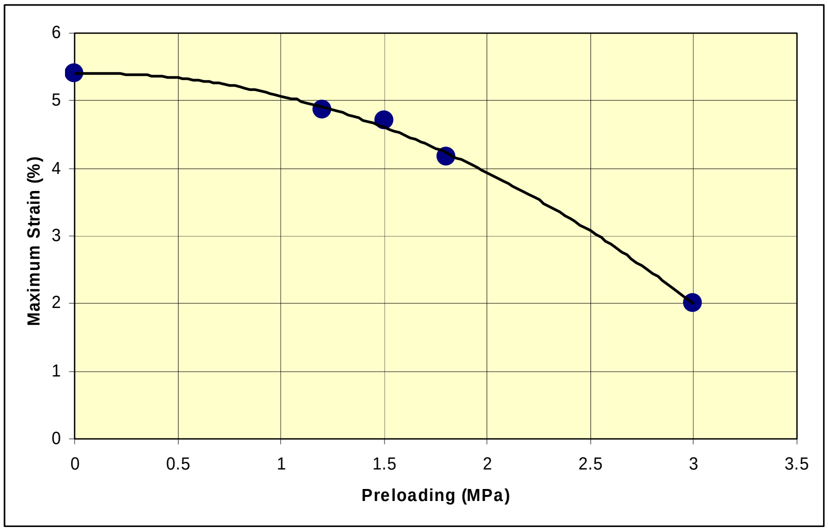

Figure 1. The maximal strain induced by a magnetic field in the MSM material as a function of the preloading applied.

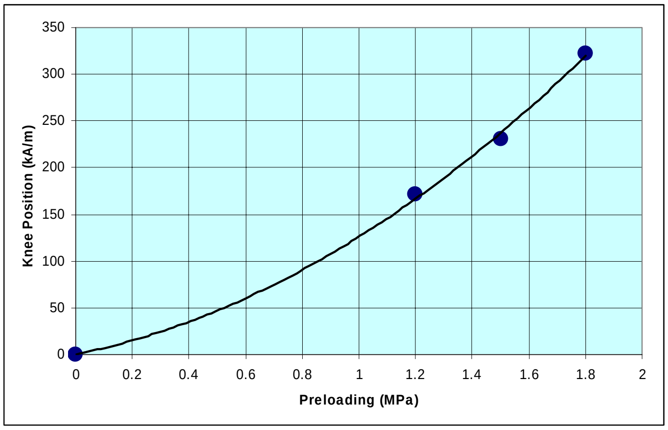

Figure 2. The position of the slope change (knee) of the strain versus field relationship as the preloading is changed for the MSM material.

Terfenol-D. Our initial fiber optic magnetometer used Terfenol-D as the sensing element. The results obtained with it are shown in Fig. 3. This interferometer used shorter wavelength (λ = 835 nm) light from a low intensity (~5 mW) red laser diode, and a photodetector constructed in our laboratory. The laser light was launched into the fiber with a Melles-Griot laser coupler, which required careful alignment. Therefore, the system was not optimized for light throughput, or for sensitivity. The solenoid used was a small prototype wound on a glass tube, which surrounded the Terfenol-D sample. This system was used as a test bed in order to obtain data which would serve to form the basis for isolating the parameters in greatest need of improvement or replacement. We replaced our laser with an infrared laser and, instead of driving it with a simple power supply and signal generator, we purchased a laser diode driver which could directly accept the modulation signal from the lock-in amplifier. These changes resulted in improvements that are evident in the data obtained later.

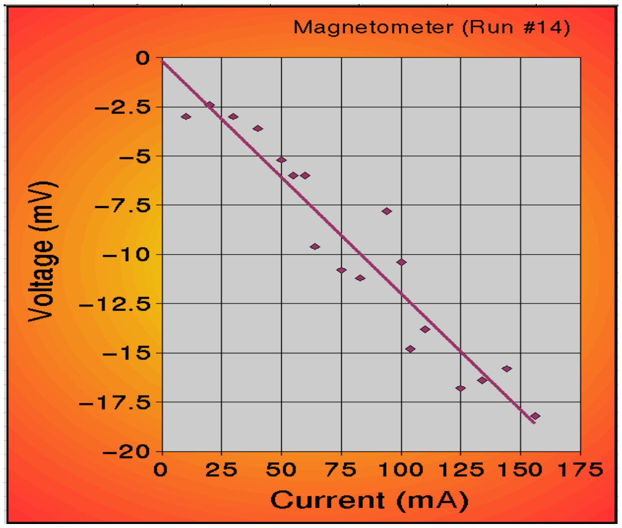

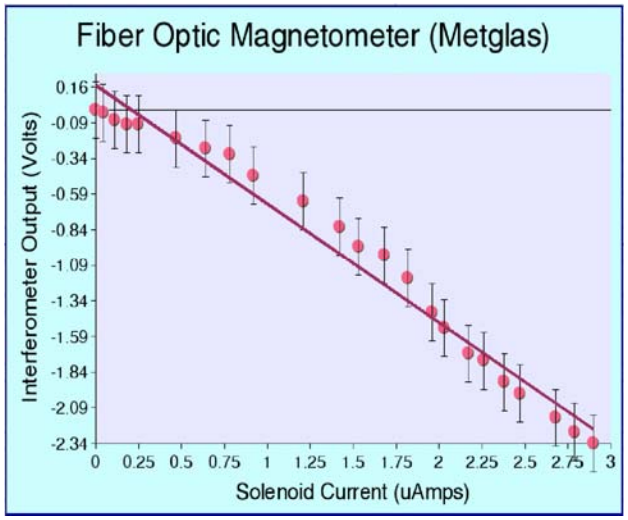

Figure 3. Performance of our magnetometer using Terfenol-D as a sensor element.

Figure 4. Performance of our magnetometer using Metglas as a sensor element.

Metglas. We obtained a large quantity of Metglas to use both for the sensor GMS material, but also for use in developing shielding for the magnetometers. We chose the annealed version of Metglas because it has a much larger magnetic permeability than the unannealed material, even though the annealed material is much more brittle. The Metglas we used has a permeability of ~40,000 so that a single layer of this shielding will reduce the background fields in our laboratory to about 1.25 nT, and two layers, separated by ~1 mm, will further reduce these fields to less than 1 pT, which was found to be completely adequate to make measurements of the performance of our GMS sensors. We illustrate this in Fig. 5 where we have measured the interferometer output during a calibration run with Metglas as the sensor, using a newer solenoid to generate the known fields. One can see that the Metglas shield has markedly reduced the noise from the background magnetic fields in the laboratory.

This system provides three orders of magnitude better output (Volts *vs.* mV) compared to the initial terfenol system (Fig. 4) and shows improved noise characteristics as well. The sensitivity we obtained was 650 mV/pT, well within range of integrated circuits, so that we can anticipate adapting this system to a miniature sensor system. The most stable material from the ones that we tested proved to be Metglas. However, Terfenol and MSM, even if they were more unstable showed a higher sensitivity and therefore their use for lung cancer diagnostic and tumor imaging seems to be feasible with the condition to ensure a proper stability in operation.

The general configuration of the sensor array is shown in Fig. 5, where the outputs from several sensors are sent into a multiplexer (MUX) and then into the signal acquistion system (DSP) for further processing. The images are generated by determining the strength of the detected field at each sensor position and then by using the calibration data to correlate the measured field intensity with the sensitivity patterns of the array. Using a sufficient number of sensors (256-512) in the array can overdetermine the field map and avoid the ambiguities posed by the use of sparser arrays.

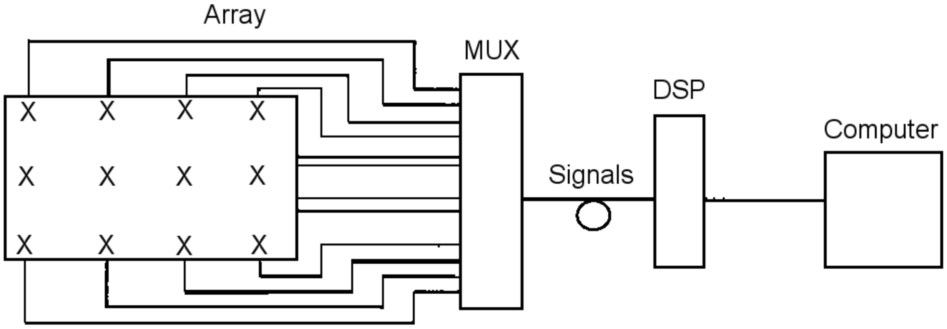

Figure 5. General Configuration of the Sensing System.

3. RESULTS

An important question about the use of nanoparticles is whether one can actually image them in living systems. Several successful reports in the literature indicate that imaging is indeed possible. For example, Weber[15] has used this method to detect tumors within a rat *in vivo*. The detected field in this case was 250 pT, well within the anticipated sensitivity requirements of our sensor array. Their results revealed that the theory of magnetic nanoparticle relaxation is basically correct.

Magnetic resonance imaging (MRI) provides good anatomical images of soft tissues without ionizing radiation. Several mechanisms for producing image contrast help distinguish diseased from healthy tissue. However, despite acceptance of MRI as a versatile and useful tool in a wide variety of clinical and research applications, imaging lung tissue is not typically performed in clinical practice. One minor difficulty is the lower proton density of lung tissue, about 25% that of other soft tissues. However, the major difficulty in imaging lung tissue is caused by small-scale magnetic heterogeneities due to the many air-water interfaces in the lung parenchyma, the tissue comprising the alveoli and small airways.[16] These small-scale heterogeneities distort the uniform applied magnetic field, resulting in rapid dephasing of the time-domain MR signal. The rapid signal decay makes it difficult to obtain good images of lung tissue using standard spin-echo or gradient-echo MR imaging sequences, which are designed for longer-lived signals. To overcome this problem, we use 3D free induction decay (FID) projection imaging[17, 18] with a sufficiently short data acquisition time to avoid image artifacts (blurring) due to the magnetic inhomogeneities. Furthermore, with FID imaging, data collection begins immediately after excitation of the proton nuclear spins (i.e., echo time = 0), such that the maximum signal intensity from the lung parenchyma is captured.

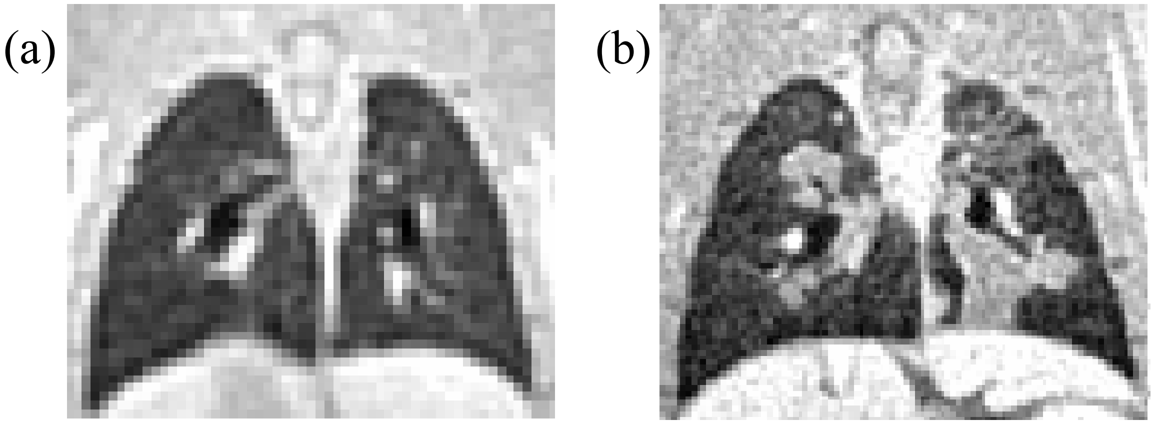

Fig. 6. FID projection MR images of two different nude rats with human lung cancer cells instilled in their large airways. The rat in (a) was imaged 1 week post-instillation (image resolution =0.74 mm). The rat in (b) was 6 weeks post-instillation (resolution= 0.37 mm).

Figure 6 shows *in vivo* T_1-weighted FID projection images of two nude rats with human lung cancer. The nude rats were irradiated to suppress their immune systems, after which Calu-6 cells (human lung adenocarcinoma) were instilled in the rats' airways and allowed to grow. The rat in Fig. 6(a) was imaged 1 week post-instillation, while the rat in Fig. 6(b) was imaged 6 weeks post-instillation. A single coronal slice has been chosen from the 3D image of each rat to show the same lung anatomy. In (a) there is little evidence of tumor growth, but in (b), large tumors are evident, appearing as bright regions emanating from the large airways (black ovals). The much denser tumor tissue (light gray) contrasts markedly with healthy lung parenchyma (dark gray). To obtain these images, we used a Harvard rodent ventilator modified to hold the rat's lungs at constant inspired volume during 0.42 s of each 1 s ventilatory cycle, and acquired data only during the constant volume period. The image parameters for Fig. 6(b) were: B_0=1.9 T, TR=3.5 ms, excitation pulse=9^o, G=60.5 mT/m, Nex=4 for each of 26850 projections, BW=1 MHz, T_{acq}=1.04 ms, total image time=30 minutes. The 9° excitation pulse fell between the Ernst angle**[19]** (in this case, 6.5°) and the tip angle for maximum T_1 weighting (10.7°), given that we measured a T_1 for rat lung parenchyma of about 1.2 s. The projections were Fourier transformed**[20]** to provide complete lines of radial k-space data at double-dense point spacing for gridding onto a 480^3 Cartesian grid. The Cartesian data were 3D Fourier transformed to yield a 480^3 image with 0.37 mm isotropic resolution that contained the rat thorax in the central 240^3 region. The image parameters for Fig. 6(a) were similar except that the gradient was decreased by a factor of two resulting in 0.74 mm resolution.

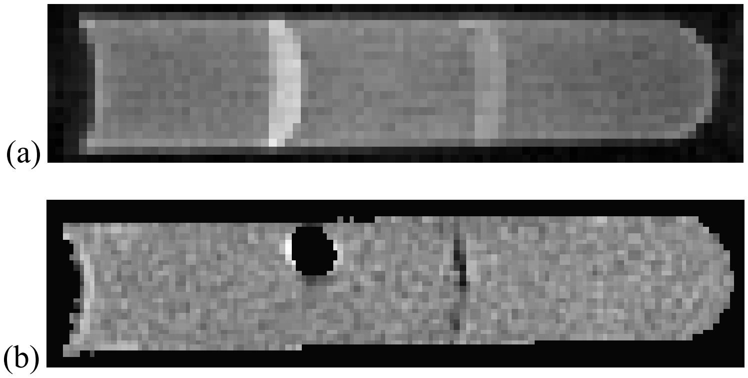

Figure 7. FID projection MR images of test tubes containing layers of human prostate cancer cells exposed to antibody-labeled magnetic nanoparticles. The images demonstrate (a) T_1-contrast and (b) phase contrast due to the presence of the nanoparticles.

Using FID projection imaging, the presence of magnetic nanoparticles can be detected by their effect on the longitudinal relaxation time T_1 of nearby protons and/or by the phase shift they cause in nearby water protons. Fig. 7(a) shows a T_1-weighted FID projection image of a test tube containing two layers of human prostate cancer cells (LNCap cells on the left, and DU145 cells on the right) sandwiched between layers of agarose gel. The cells have been exposed to magnetic nanoparticles that we labeled with an antibody targeted to the LNCap cells. Although the cell layers and the agarose gel have nearly the same density of proton spins, the LNCap cells appear significantly brighter in the image due to their shorter recovery time T_1. Some non-specific binding to the DU145 cells is also apparent. Fig. 7(b) shows an FID projection phase image of a similarly-prepared sample; in (b), the DU145 cells are on the left, near the air bubble, and the LNCap cells are on the right. Here, the preferential binding of the antibody-labeled magnetic nanoparticles to the LNCap cells is evident in the phase image as a dark band, and binding to the DU145 cells is not detectable. In this case, the antibody-labeled magnetic nanoparticles had a larger diameter, resulting in transverse relaxation time (T_2)-contrast observed in spin-echo images (not shown) and the phase contrast observed in Fig. 7(b), but no T_1-contrast. We expect to observe T_1 and phase contrast, similar to that in Figs. 7(a) and (b), in T_1-weighted FID projection images of lung cancer cells exposed to antibody-labeled magnetic nanoparticles (described in Section 1), both *in vitro* and *in vivo*. We therefore anticipate that FID projection imaging of rat lungs will be useful for showing us the anatomical location of the magnetic nanoparticles for comparison with magnetic images made using the array magnetometer.

4. INVERSE RECONSTRUCTION OF THE SOURCE

The problem of determining a current density confined to a volume from measurements of the magnetic and electric fields it produces exterior to that volume is known to have nonunique solutions[21, 22, 23, 24]. Despite this nonuniqueness, in previous work we have shown that one may uniquely determine certain moments of the vector spherical harmonic expansion of the current[25]. We have demonstrated that the determination of these moments allows for the unique inversion of a current density confined to a spherical shell. By employing a regularization procedure to carry out faithful inversions in the presence of noise which is amplified selectively at high frequencies due to the ill-conditioned character of the inversion (Fig 8). Numerical implementation in terms of scalar spherical harmonics has resulted in a robust algorithm with good resolving power, even in the presence of substantial noise. Our current work seeks to extend this reconstruction methodology and study its implications for clinically useful fast Magnetic Imaging. We have recently demonstrated the uniqueness of inversion for the case of a current confined to a star-shaped shell. The formalism employed in our equivalent surface current reconstruction can be used without change to determine a surface dipole source density consistent with the measured magnetic field. Considering shells with other than spherical shapes adds a degree of freedom in the reconstruction which may help better localize the sources in a practical situation.

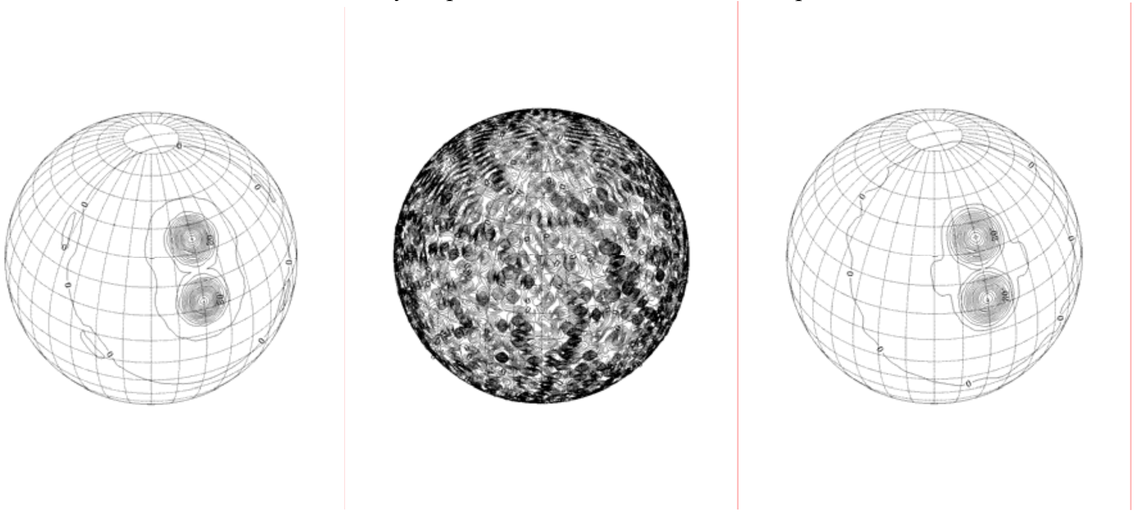

Figure 8: Inversion of a model current source Left: reconstruction (indistinguishable from noise-free original). Middle: unfiltered reconstruction from same original with 5% Gaussian Noise. Right: same as middle but with filtered reconstruction

AKNOWLEDGEMENTS

The authors are grateful to the National Institutes of Health – National Cancer Institute for the financial support offered under an STTR grant for performing this research. The authors also thank Kevin Divine, Sebastian Bredow, and Dolores Esparza, Lovelace Respiratory Research Institute, for preparation and care of the rats with lung cancer. The authors also thank Rita Serda, University of New Mexico, for preparing the antibody-labeled nanoparticles and prostate cancer cell samples.

REFERENCES

1. Shimizu, N., Ando, A., Teramoto, S., Moritani, Y., and Nishii, K. Outcome of patients with lung cancer detected via mass screening as compared to those presenting with symptoms. J. Surg. Oncol. 50(1992)7
2. Bonomi, P. "Non small cell lung cancer chemotherapy." In Pass, H. I., Mitchell, J. B., Johnson, D. H., and Turrisi, A. T. (eds.) Lung Cancer: Principles and Practice. Lippincott (Philadelphia: 1996) p. 811.
3. Johnson DH, Greco FA. Small cell carcinoma of the lung. Crit Rev Oncol Hematol. 4 (1986)303-336.
4. Johnson D. H. Chemotherapy of small cell lung cancer. In Pass, H. I., Mitchell, J. B., Johnson, D. H., and Turrisi, A. T. (eds.) Lung Cancer: Principles and Practice. Lippincott (Philadelphia: 1996) p. 825.
5. Arriagada R, Le Chevalier T, Pignon JP, Riviere A, Monnet I, Chomy P, Tuchais C, Tarayre M, Ruffie P. Initial chemotherapeutic doses and survival in patients with limited small-cell lung cancer. N Engl J Med. 329(1993)1848-1852.
6. Popa, S.G., Sillerud, M., Shahinpoor, M., Smart Fiber Optic Magnetometer Array for MEG, World Congress of Biomimetics and Artificial Muscles, December 2002, Albuquerque, NM
7. Sillerud, L.O., Popa, S.G., Coutsias, E.A., Computer Aided Solution of the Inverse Field Problem for High Sensitivity Biomagnetometry. Biocomputing@UNM Workshop, April 12, 2004, Albuquerque, NM
8. Lyda MH, Weiss LM. Immunoreactivity for epithelial and neuroendocrine antibodies are useful in the differential diagnosis of lung carcinomas. Hum Pathol. 2000 Aug;31(8):980-7.
9. Cornfield D, Liu Z, Gorczyca W, Weisberger J. The potential role of flow cytometry in the diagnosis of small cell carcinoma. Arch Pathol Lab Med. 127 (2003)461-464.
10. Epstein C, Lynch T, Shefner J, Wen P, Maxted D, Braman V, Ariniello P, Coral F, Ritz J. Use of the immunotoxin N901-blocked ricin in patients with small-cell lung cancer. Int J Cancer Suppl. 8(1994)57-59.
11. Roy DC, Ouellet S, Le Houillier C, Ariniello PD, Perreault C, Lambert JM. Elimination of neuroblastoma and small-cell lung cancer cells with an anti-neural cell adhesion molecule immunotoxin. J Natl Cancer Inst. 88(1996) 1136-1145.
12. Lynch TJ Jr, Lambert JM, Coral F, Shefner J, Wen P, Blattler WA, Collinson AR, Ariniello PD, Braman G, Cook S, Esseltine D, Elias A, Skarin A, Ritz J. Immunotoxin therapy of small-cell lung cancer: a phase I study of N901-blocked ricin. J Clin Oncol. 15(1997) 723-34.
13. Weitschies W, Kotitz R, Bunte T, Trahms L. Determination of relaxing or remanent nanoparticle magnetization provides a novel binding-specific technique for the evaluation of immunoassays. Pharm. Pharmacol. Lett. , 1997, 7 , pp. 1-7
14. L. G. Remsen, C. I. McCormick, S. Roman-Goldstein, G. Nilaver, R. Weissleder, A. Bogdanov, I. Hellstrom, R. A. Kroll and E. A. Neuwelt, American Journal of Neuroradiology 17, 411 (1996)
15. Weber, P., Romanus, E., Warzemann, L., Prass, S., Gross, C., Huckel, M., Brauer, R., and Weitschies, W. http://www.maschinenbau.tu-ilmenau.de/mb/wwwtd/hydromag/ferro/ conferences/workshops/benediktbeuern/pdfs/weber.pdf.
16. Ailion, D. C. "Introduction to MRI Techniques Used in Lung" in Cutillo, A. G. (ed.) Application of Magnetic Resonance to the Study of Lung. Futura (Armonk, NY: 1996).
17. Kuethe, D. O., Caprihan, A., Fukushima, E., and Waggoner, R. A. Imaging Lungs Using Inert Fluorinated Gases. Magn. Reson. Med. 39(1998)85-88. (Sorin's ref. 21)
18. Glover, G. H., Pauly, J. M., and Bradshaw, K. M. Boron-11 Imaging with a three-dimensional reconstruction method. J. Magn. Reson. Imaging 2(1992)47-52.
19. Fukushima, E. and Roeder, S. B. W. Experimental Pulse NMR: A Nuts and Bolts Approach. Addison-Wesley (Redwood City, CA:1981), pp. 446-8.

20. Kuethe, D. O., Caprihan, A., Lowe, I. J., Madio, D. P., and Gach, H. M. Transforming NMR Data Despite Missing Points. J. Magn. Reson. 139(1999)18-25.
21. Ioannides, A.A., Bolton, J.P.R., and Clarke, C.J.S., Continuous probabilistic solutions to the biomagnetic inverse problem, Inverse Problems 5 (1989), 999-1012
22. Liitkenhoner, B., On the biomagnetic inverse procedure's capability of separating two current dipoles with a priori known locations, in Advances in Biomagnetism: Clinical Aspects, Excerpta Medica, M. Hoke, S.N. Ern6, Y.C. Okada, and G.L. Romani, eds., Amsterdam, 1992, 687-692
23. Menninghaus, E., Liitkenhoner, B., Gonzalez, S.L., Hampson, S., and Pantev, C., Localization of a dipolar source in a skull phantom: Comparison between boundary element model and spherical model, in Proceedings of the Satellite Symposium on Neuroscience and Technology of the 14th International Conference of the IEEE Engineering in Medicine and Biology Society, A. Dittmar and J.C. Froment, eds., Lyon, 1992, 119-122
24. Purcell, Christopher J., and Stroink, Gerhard, Moving dipole inverse solutions using realistic torso models, IEEE Trans. Biomed. Eng. BME38 (1991), 82-84
25. Sheltraw, Daniel, and Coutsias Evangelos A., J. Appl. Phys. 94(2003)#9